Journal of Membrane Science 641 (2022) 119898

Contents lists available at ScienceDirect

Journal of Membrane Science

journal homepage: www.elsevier.com/locate/memsci

Capillary bonding of membranes by viscous polymers: Infiltration kinetics and mechanical integrity of the bonded polymer/membrane structures

Jaylene Martinez [a], Masoud Aghajani [a], Yinan Lu [a], Adrienne K. Blevins [b], Shouhong Fan [a], Mengyuan Wang [a], Jason P. Killgore [c], Stefano Berti Perez [d], Jaivin Patel [d], Christina Carbrello [d], Sean Foley [d], Ryan Sylvia [d], Rong Long [a], Robert Castro [d], Yifu Ding [a,b,*]

[a] Membrane Science, Engineering and Technology Center, Paul M. Rady Mechanical Engineering, University of Colorado at Boulder, Boulder, CO, 80309-0427, USA
[b] Material Science & Engineering Program, University of Colorado at Boulder, Boulder, CO, 80309, USA
[c] Applied Chemicals and Materials Division, National Institute of Standards and Technology, Boulder, CO, 80305, USA
[d] MilliporeSigma, 80 Ashby Rd. Bedford, MA, 01730, USA

ARTICLE INFO

Keywords:
Capillary infiltration
Porous membranes
Bonding strength
Mechanical properties of membranes

ABSTRACT

Capillary infiltration of porous medium impacts applications across oil recovery, soil science, and hydrology. The infiltration kinetics is typically captured by a range of models that differ in the approximation of pore structures, fluid properties, and filling ratio. Capillary bonding of a porous membrane by a polymer melt is important for membrane device manufacturing. However, both the capillary infiltration kinetics and the resulting bonding strength or mechanical integrity have not been reported. In this work, we measure the kinetics of capillary infiltration of a viscous polypropylene (PP) in polyethersulfone (PES) membranes with a normal pore size of 200 nm and varying degrees of hydrophilicity. The time-dependent infiltration depth was quantified *ex situ* by imaging the cross-sections of the bonded PP film/PES membranes. The microscopic details of the bonded interface were characterized by high-resolution nanomechanical imaging, while the contact angles of PP on the PES surfaces were measured by the sessile droplet method. The results show that the infiltration kinetics at 180 °C is better described by the Cai model that incorporates membrane pore structures (porosity, tortuosity, pore size), compared with the basic Lucas Washburn model intended for isolated cylindrical pores. The infiltration kinetics at 200 °C appears significantly slower than the predictions of both models, which is hypothesized to be a result of pore deformation/collapse due to the capillary pressure when the PES approaches the rubbery state. Regardless of bonding temperature, the resulting mechanical integrity of the bonded PP film/PES membrane, as quantified by a modified T-peel test, is dictated by the fracture strength of the membranes and weakly decreases with the increase of infiltration depth.

1. Introduction

Tremendous progress has been made in developing novel chemistries [1–6] and functional surfaces [7–11] to achieve better permselective performances for membrane technologies. To integrate these high-value-added membranes into functional filtration device format(s), controlled bonding between the membranes with the supporting structures (typically thermoplastic polymers) must be achieved. Failure to do so can result in manufacturing yield loss or product failure during applications such as biopharmaceutical manufacturing and buildings. For example, membranes used in HVAC systems in building applications must be reliably bonded into supporting housing structures. As such, the limitation in membrane-to-component bonding has been identified as one of the top challenges for applying membrane technologies in building applications [12]. Among the different bonding methods, thermal wielding uses infiltration of a polymer into the membrane pores, driven by either capillary force or external pressure. Capillary bonding process is relatively slow but does not densify the membrane. Currently, both the capillary infiltration kinetics of viscous polymers within separation membranes and the resulting mechanical integrity of the bonded polymer/membrane structure has not been reported in literature.

Capillary infiltration or imbibition of polymer fluids within cylindrical pores such as anodic aluminum oxide (AAO) membranes has been

* Corresponding author. Membrane Science, Engineering and Technology Center, Paul M. Rady Mechanical Engineering, University of Colorado at Boulder, Boulder, CO, 80309-0427, USA.
E-mail address: yifu.ding@colorado.edu (Y. Ding).

https://doi.org/10.1016/j.memsci.2021.119898
Received 26 July 2021; Received in revised form 11 September 2021; Accepted 18 September 2021
Available online 21 September 2021

Nomenclature

List of symbols

t	time in seconds
R	average pore radius of the membrane
T	Acrylate modified PES (PES_T)
M	Acrylamide modified PES (PES_M)
U	Unmodified PES (PES_U)
T_m	melting temperature
T_g	glass transition temperature
R_g	radius of gyration of the polymer
S_w	Pore saturation ratio
S_i	pre-pore filling
D_f	fractal dimension
R_{max}	maximum pore radius of the membrane
E	Young's Modulus
E^*	Effective Young's modulus of a membrane
E_o	Young's modulus of a bulk polymer
C_1	constant
C_2	constant

Greek letters

γ	surface tension
θ_E	Equilibrium contact angle
η_o	Steady-state viscosity
σ_y	Yield Strength
χ	Flory-Huggins interaction parameter
σ^*	yield strength of the membrane
σ_0	yield strength of the polymer
ρ^*	density of the membrane
ρ_0	density of the bulk polymer
φ	porosity
τ	tortuosity
α	geometry factor of the pore shape
δ_{PES}	solubility

Subscripts

PES	Polyether sulfone
PP	Polypropylene
$PP-PES$	Between PP and PES

broadly investigated [13,14]. The infiltration kinetics is controlled by the capillary pressure and viscous drag, as described by the Lucas-Washburn (LW) equation [15,16].

$$L(t) = [(R\gamma cos\theta_E/2\eta_0)t]^{1/2} \quad (1)$$

where $L(t)$ is the infiltration depth within the porous medium, γ and η_0 are surface tension and viscosity of the fluid, and θ_E is equilibrium contact angle of the fluid on the pore wall. For AAO membrane with average pore radius (R) ranging between 300–900 nm, polymers such as polystyrene (PS) can infiltrate the membranes (100 μm thick) within minutes depending on temperature [13,14]. However, the polymers only wet the cylindrical walls of the pores and form nanotubes after etching away the AAO membrane. In other words, the pore saturation ratio remains low. Another study systematically examined the kinetics of the capillary filling of polyethylene (PE) in AAO membrane (60 μm thick, 100 and 200 nm pore radius) [17]. At 130 °C, slightly above the melting temperature (T_m) of PE, capillary filling kinetics were found to deviate from typical LW prediction, which was attributed to the non-linear flow of the PE. The effective viscosity is found to be ~3–4 times lower than η_0.[18] Conflicting observations have been made on the polymer dynamics and kinetics of capillary filling of smaller pores. Under strong confinement, i.e. $2 < R/R_g < 6$, where R_g is the radius of gyration of the infiltrating polymer, significantly reduced filling rate was observed: it took 4 days for an entangled polybutadiene (PB) to completely fill the 100 μm thick AAO membrane [19]. Further, the dynamics of the adsorbed PB layer appears to be independent of temperature and network-like, which is interpreted by the reptation model.

Reports can be found on capillary infiltration of polymers within porous media with non-cylindrical pores including densely packed silica nanoparticles (NP) films [20] and porous silicon (Si) membrane [21]. Under strong confinement, i.e. $0.3 < R/R_g < 4.5$, dramatic slow-down of the PS infiltration in the silica NP films was observed: the apparent viscosity estimated from the LW equation was nearly two-orders of magnitude higher than bulk viscosity. This slow-down was attributed to the increase in T_g of PS due to strong confinement.

Capillary infiltration of porous Si membrane with ethyl vinyl acetate copolymer (EVA) was recently examined [21]. Compared with the AAO membranes and nanoparticle layers, porous Si membrane resembles separation membranes, in terms of both porosity ($\varphi = 68 - 84\%$) and pore connectivity. The infiltration rate of EVA was found to be sensitive to temperature. Within minutes, infiltration of 15 μm thick porous Si membrane was achieved. With the strong confinement, i.e. $0.1 < R/R_g < 3$, enhanced mobility was observed, in contrast to the slow-down observed in earlier studies.

In comparison, capillary infiltration of non-polymeric fluids in random porous media is well investigated for applications of oil recovery, soil science and hydrology. In most of these studies, experimentally determined infiltration kinetics are slower than the predictions of the LW model. Accordingly, a host of modified LW-type models have been developed to take into consideration complex porous structures [22,23]. Most of these models still bear the same $t^{1/2}$ behaviors as the LW model, but incorporate pore-structures to account for the delayed kinetics. For example, a representative tortuous capillary model (the Cai model) uses fractal dimension, D_f, together with φ and tortuosity (τ), to describe the infiltration kinetics [23].

$$L(t) = \frac{\varphi(S_w - S_i)\alpha^{\frac{3}{2}}}{\tau}\left(\frac{D_f}{4 - D_f}\right)^{1/8}\left(\frac{R_{max}\gamma cos\theta_E}{2\eta}t\right)^{1/2} \quad (2)$$

where S_w and S_i are the degree of saturation and initial wetting fraction of the pores, and α is geometry correction factor (=1 for a cylindrical cross-section). Notably, the use of this model to predict capillary infiltration of polymers in porous membranes has not been reported.

To date, capillary infiltration of polymeric fluids in polymeric porous membranes such as typical ultrafiltration (UF) and microfiltration (MF) membranes have not been examined in open literature. Compared with the AAO membranes and the NP films, MF and UF membranes have significantly higher porosity, as well as interconnected pores. MF and UF membranes often have gradients in both pore size and porosity, resulting from different manufacturing processes. Furthermore, membranes with different pore chemistry (e.g. hydrophilicity) are desired for specific applications. It is unclear how these structural and chemical factors impact the capillary infiltration in porous membranes. In addition, it is unclear how different degrees of infiltration of polymer impact the bonding strength or mechanical integrity of the resulting device. In this response, this study examines the process of polymer film filling porous membranes. The effects of membrane chemistry and bonding temperature on the infiltration kinetics are systematically examined. The experimental data is analyzed with both LW model and the Cai model. Further, the correlation between infiltration depth and mechanical integrity of the bonded polymer/membrane structure is quantified.

2. Experimental methods

2.1. Materials and characterizations

Polyether sulfone (PES) asymmetric membranes with a nominal pore size rating of 200 nm are fabricated using non-solvent induced phase separation (NIPS) process. Three different membrane chemistries are prepared with increasing degree of hydrophilicity: unmodified (PES_U), modified with acrylate (PES_T) and modified with acrylamide (PES_M). Such a series of membranes present identical pore structure but varying pore chemistry. The average membrane thickness for all three membranes is similar (≈184 μm).

Isotactic polypropylene (PP) polymerized with metallocene catalysis is used as the infiltrating polymer. The molecular weight, as determined using rheology measurement data and Rheology Polymer Library (Trios software package, TA Instruments Rheometer, Model ARES-G2), is 2.09 $\times 10^5$ g/mol, and the polydispersity index (PDI) is 1.83.

The thermal properties of PP film (200 μm thickness) were characterized by differential scanning calorimetry (DSC, 204 F1 NETZSCH, Germany). PP film (~5 mg) was sealed in an aluminum pan and kept at 20 °C for 5 min, and subsequently heated from 20 to 200 °C at a rate of 5 °C/min. The T_m and the heat of fusion (ΔH_m) of the PP were determined as the peak temperature and the total area of the melting endotherm. The crystallinity (X_c) of the PP was then calculated according to the following equation,

$$X_C = \frac{\Delta H_m}{\Delta H^*} \times 100\% \quad (3)$$

where ΔH^* (= 170 J/g) [24] is the heat of fusion of a 100% crystalline PP.

The viscosity of the PP film, at both capillary bonding temperatures, 180 and 200 °C, was measured using rheometer (AR-G2, TA Instruments). The measurements were carried out using parallel plates configuration with 8-mm diameter plates. The gap distance between testing plates was kept at 200 μm and the viscosity of the PP film was measured as a function of shear rate from 0.001 to 150 s^{-1}. The average values of the steady-state viscosity from three samples are reported.

The temperature-dependent mechanical properties of PES membranes and PP film were determined using a dynamic mechanical analysis (DMA, Q800, TA Instruments). The samples were cut into 20 mm × 5 mm strips for all the measurements. Average values from three measurements are reported here. All the tests were conducted under normal tensile loading at a frequency of 1 Hz with a strain amplitude of 1%. After being equilibrated at 50 °C for 5 min, the temperature was ramped to 250 °C with a ramping rate of 3 °C/min for the PES membrane samples and to 165 °C at a rate of 3 °C/min for the PP film.

The contact angle of molten PP liquid on solid PES surfaces with three different chemistries was determined using sessile drop method at 200 °C. Dense PES films were created by densifying the three PES membranes at 200 °C under high pressure. A PP bead was prepared and placed atop the PES surfaces and heated to 200 °C in a vacuum oven for 24 h to allow sufficient spreading of the PP on the PES. The contact angle was imaged after the sample was cooled down to room temperature. Three measurements were carried out for each PES surface chemistry and the average values with standard deviations are reported.

2.2. Capillary bonding of PP film with PES membranes

For all the bonding experiments, the PP film was in direct contact with the smaller-pore side of PES membranes. For the capillary infiltration kinetics study, the size of both the PES membrane and PP film was 1.6 cm × 1.4 cm (L × W). The PP film/PES membrane assembly was then sandwiched between two glass slides and placed in a pre-heated oven (temperature calibrated at 180 °C and 200 °C) for a prescribed amount of time. A convection oven (Fisher Scientific Isotemp) was used for bonding at 200 °C for 0.25 h, 0.5 h, and 1 h, as well as at 180 °C for 0.05 h, 0.25 h, 0.5 h and 3 h. A vacuum oven (Fisher Scientific Isotemp model 281A) was used for all the other bonding experiments at 200 °C for 4 h, 12 h, 24 h and at 180 °C for 6 h, 9 h, 12 h and 24 h. The infiltrated samples were then quickly cooled to room temperature and used for later characterizations.

The samples for mechanical integrity test were prepared using the approach illustrated step-by-step in Fig. 1. (a) Three PES membranes (duplicates) with size of 9.2 cm × 1.4 cm (L × W) were placed onto a Kapton film (chosen for its high thermal stability) atop a glass slide. (b) A smaller Kapton film (5.1 cm × 2.5 cm) was placed atop the PES samples to cover 50% of the PES membrane samples. (c) Three PP film strips with size of 8.9 cm × 1.3 cm (L × W) were placed atop PES/Kapton film. The Kapton film creates 50% non-contact area in PP and PES membranes, which is necessary for fixation in T-peel test later. (d) All samples were then covered with another Kapton film to prevent adhesion to the top glass slide. The assembly was then placed in the pre-heated oven for prescribed times to create capillary bonding.

2.3. Characterization of infiltrated PP film/PES membrane regions

Cross-sections of the PP film/PES membrane samples were prepared at room temperature using a Leica Microsystems cryoultramicrotome (model EMUC7) with an ultra AFM MT16182 Diatome blade (a feed of 200, with a speed of 3 mm/s). The microtomed cross-sections are smooth enough for precise determination of infiltration depth using an optical microscope (OM, Olympus BX60). Under microscope, the PP, PES, and PP film/PES regions can be clearly distinguished due to their difference in light scattering/reflection. The infiltration depth was quantified using Infinity Analyze software based on the images obtained and length scale calibrated with standard samples. Due to the limit of the OM resolution, infiltration depths that are lower than 10 μm (corresponding to short-time infiltration) were not investigated.

To obtain microscopic pore-level details of the bonded interface, PP film/PES membrane bonded at 180 °C for 3 min was imaged with atomic force microscope (AFM). The microtomed sample was mounted into an AFM (Cypher, Asylum Research) with the cross-section in contact with the AFM tip. Prior to any measurements, optical images were taken of the microtomed surfaces using the AFM's built-in optics system to locate the bonded interface. Topographic scans and force-volume mapping measurements were taken along the PES membrane _PP film/PES membrane _PP film tri-layer regions. To image all three regions with sufficiently high resolution, multiple scans were carried out to construct one image. All scans were performed using a cantilever (PPP-NCHAuD, Nanosensors) with a nominal force constant of 42 N/m and nominal resonance frequency of 330 Hz. For force mapping, the AFM was operated in Fast Force Mapping (FFM) mode to quickly perform force curves at each point of the scan, which had a pixel size of 9.2 nm. An indentation force of 150 nN was used. The standard Hertz contact model with a 10 nm tip radius value was used to calculate surface modulus values for each force curve, resulting in a spatially resolved modulus map of the sample surface [25,26].

2.4. Mechanical integrity test of the bonded PP film/PES membrane samples

The mechanical integrity of the bonded PP film/PES membrane was measured at room temperature using a modified T-peel test (ASTM-D1876) using an Instron 5965 with a 5 kN load cell. The non-bonded regions of the PP film and PES membrane were mounted onto the top and bottom grips of the Instron machine to create the T-peel test condition. The T-peel test samples were loaded until the non-bonded PP film and PES membrane were straightened and aligned vertically with a 180° angle between them. Next, the samples were pulled under a constant velocity of 5 mm/min until failure. The force-displacement curves were recorded, and the peak force was used as an effective measure of the

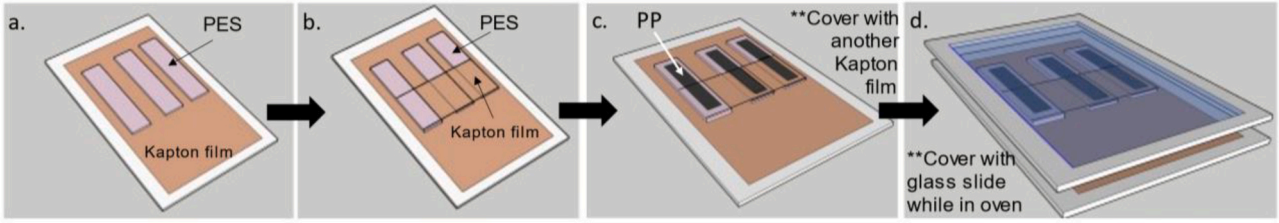

Fig. 1. Schematic of sample preparation for the T-peel test: (a) PES membranes (3 duplicates) were placed onto a Kapton film supported by a glass slide. (b) A Kapton film was placed on the PES membranes to cover 50% of each PES sample. (c) PP films (3 strips) were placed atop PES membranes. (d) The assembly in (c) was then covered with another Kapton film and then a glass slide for the subsequent thermally induced capillary bonding experiments.

mechanical integrity.

3. Results and discussions

3.1. Thermomechanical and rheological properties of the PP film and PES membranes

The properties of both PP film and PES membranes, which are important to both the bonding process and the resulting mechanical integrity are each characterized and summarized in Tables 1 and 2, respectively. From DSC measurement, PP film has a melting temperature, T_m of ≈156 °C and a $\Delta H_m = 98.6$ J/g. Based on Eq. (3) with $\Delta H^* = 170$ J/g for 100% iPP crystalline [24], the iPP film used in this study has a crystallinity value of $X_c = 58.0$ %. Accordingly, PP is a typical semi-crystalline thermoplastic polymer at room temperature. From uniaxial tensile test (Fig. 2A), the PP film has a Young's modulus (E) of ≈200 MPa, a yield strength (σ_y) of 9.52 ± 2.4 MPa, and a strain-at-failure of greater than 500% (not shown in Fig. 2 for clarity). The combination of toughness, thermal stability, hydrophobicity, and cost-effectiveness makes PP a common polymer for existing membrane devices and potential for membrane technologies in building applications.

Thermomechanical properties of PES membranes are more complex due to the porous structure. The porosity of the three membranes (i.e., PES_U, PES_M and PES_T) was measured (by mass and volume measurements) to be ~80%. Chemical modification did not result in measurable alteration in porosity. Fig. 2a shows the uniaxial tensile stress-strain curves for all three membranes, from which effective Young's modulus (E^*), yield strength (σ^*), and strain-to-failure are obtained and summarized in Table 2. From prior studies, the E^* and σ^* of UF and MF membranes can be described by open-cell foam analysis developed for macroscopic porous materials [27–29].

$$E^* = E_o C_1 (\rho^*/\rho_0)^2 \quad (4)$$

$$\sigma^* = \sigma_0 C_2 (\rho^*/\rho_0)^{3/2} \quad (5)$$

where E_0 (or σ_0) are the Young's modulus (or yield strength) of the bulk polymer; ρ^* and ρ_0 are the density of the membrane and bulk polymer, respectively; C_1 is a constant (≈1), while C_2 is a constant between 0.2 and 0.3. Using $E_0 = 2.4$ GPa (at 40 °C) [30], $C_1 = 1$, $\rho^*/\rho_0 = 0.2$ (porosity = 80%), E^* is calculated to be 98 MPa, which falls between the values obtained from uniaxial tensile tests (Table 1) and DMA (≈120 MPa). Similarly, σ^* is calculated to be 1.76 MPa, using $\sigma_0 = 78.9$ *MPa* [30] and $C_2 = 0.25$, which is also similar to the experimental value (1.7–2 MPa, Table 2).

DMA measurement on PES membranes (only PES_M is shown in Fig. 2b for clarity) show that the T_g of the PES was ≈210 °C, as commonly reported for PES [28]. Based on these characterizations, the capillary bonding temperature used are 180 °C and 200 °C, which falls between the T_m of PP film and T_g of PES. Rheological properties of the PP film at both 180 °C and 200 °C are examined (Fig. 3) with the steady-state viscosity, η_0 is measured to be 1650 Pa s and 290 Pa s, correspondingly. From the shear rate dependency of the PP film at both temperatures, onset of shear thinning, or nonlinear flow occurs at frequency higher than 10 s^{-1} at 180 °C and 200 °C (Fig. 3). Therefore, the PP film can be considered Newtonian during the infiltration at both temperatures, as the chain relaxation time (<1 s, according to the onset of shear thinning in Fig. 3) is significantly shorter than the overall infiltration time used in the study (ranging from 3 min to 48 h).

Table 1
Properties of PP film.

γ_{PP}[a] (mJ/m^2)	T_m (°C)	E (MPa)	σ_y (MPa)	Failure strain (%)	η_0 200 °C (Pa·s)	η_0 180 °C (Pa·s)	CA (degree)
20	156	200	9.5	>500%	290	1650	100

[a] From ref. 22.

3.2. Miscibility and wettability of PP film and PES membrane

PP is immiscible with PES as evidenced from their large difference in solubility parameter. The solubility parameter of PP ($\delta_{PP} \approx 16.6$ MPa$^{1/2}$) [31] is significantly lower that of the PES ($\delta_{PES} \approx 23$ MPa$^{1/2}$) [32]. From the Hilderbrand equation, the Flory-Huggins interaction parameter, χ_{PP-PES} at 200 °C is estimated to be ~0.48. For such a high value of χ, the mixing free energy between PES and PP is expected to be positive for chains that are longer than 10 repeating units. In other words, no mixing is expected between PP film and PES membrane throughout the bonding and testing. The fundamental interfacial interaction between PP film and PES membrane is expected to be entirely long-range van der Waals bonding.

From water contact angle (CA) measurements, PP film is a typical hydrophobic polymer with CA = 100° (Table 1). The hydrophilicity of PES membrane increases in the order of PES_U, PES_T, and PES_M, consistent with the hydrophilicity of the monomers used to functionalize the membrane surfaces. To understand the capillary infiltration kinetics, the wettability of PP film on PES membrane is needed, which can be characterized by directly measuring the contact angles of PP on dense PES films, θ_{PP-PES}. Using the sessile droplet method (i.e. equilibrating a PP droplet on a PES film at 200 °C in vacuum for 24 h), θ_{PP-PES} at 200 °C were determined to be 12°, 14.5°, and 14.7° for PES_U, PES_M, and PES_T respectively. The data confirms that PP can preferentially wet all three PES chemistries.

It is worth noting that θ_{PP-PES} obtained above allow estimation of the interfacial tension between PP and PES, γ_{PP-PES}, whose values have not been reported in literature to the best of our knowledge. The estimation is based on the Young's equation,

$$cos\theta_{PP-PES} = \frac{\gamma_{PES} - \gamma_{PP-PES}}{\gamma_{PP}} \quad (6)$$

where γ_{PP} and γ_{PES} are the surface tension of PP and PES, respectively. From literature, $\gamma_{PP} = 20$ mJ/m^2 at 200 °C [33], while $\gamma_{PES} = 47$ mJ/

Table 2
Properties PES membranes.

Membrane	φ(%)	E* (MPa)	σ^*(MPa)	Failure strain (%)	γ_{PES}(mJ/m^2)	δ_{PES} (MPa$^{1/2}$)	θ_{PP-PES}
PES_U	80	58.1 ± 1.3	1.7	16%	47	23	12.0
PES_M	80	67.9 ± 1.6	1.9	27%	–	–	14.5
PES_T	80	79.3 ± 1.6	2.3	16.5%	–	–	14.7

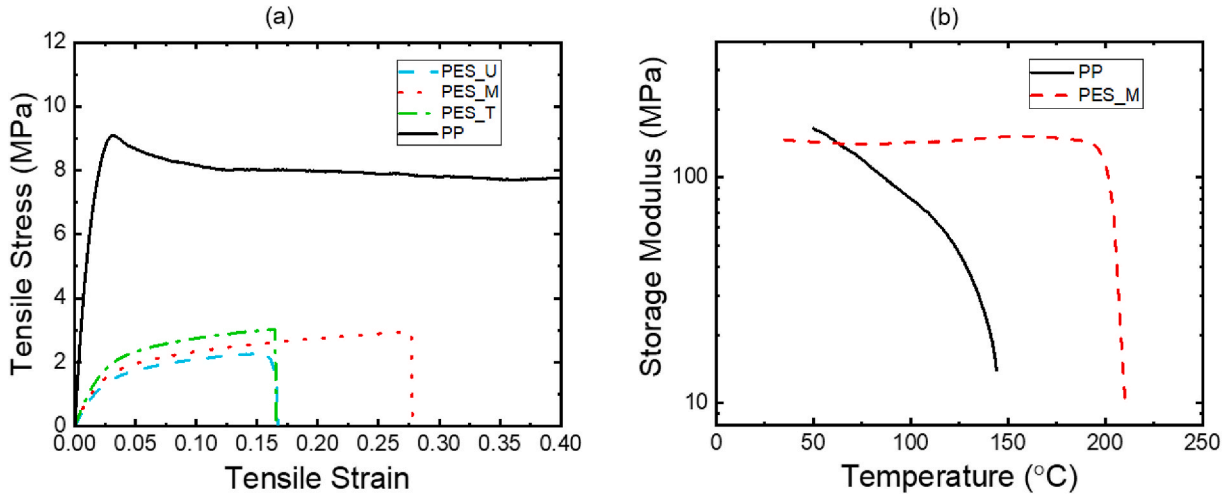

Fig. 2. (a) Uniaxial tensile stress-strain curves for PP and three PES membranes at room temperature, under uniaxial tensile loading. (b) Storage modulus as a function of temperature for PP and PES_M, obtained from DMA measurements with a frequency of 1 Hz.

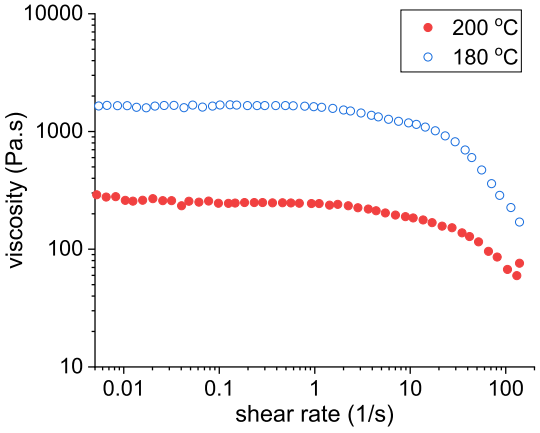

Fig. 3. Viscosity as a function of shear rate for PP at 180 °C and 200 °C.

m^2 [34] at room temperature. Assuming $\frac{d\gamma}{dT} \approx 0.06$ mJ/(m^2·K), as commonly observed for most engineering plastics [33,35], the γ_{PES} would be 36.2 mJ/m^2 at 200 °C. Accordingly, γ_{PP-PES} at 200 °C is estimated to be ~16.6 mJ/m^2, 16.9 mJ/m^2, and 16.8 mJ/m^2 for PP in contact with PES_U, PES_T, and PES_M surfaces, respectively. These values estimated here are similar to the reported interfacial tension between PP and polycarbonate (surface tension close to PES) at 225 °C (=17.4 mJ/m^2) [36]. Nevertheless, above analysis confirms that PP film preferentially wets PES with all three membrane chemistries, which allow capillary infiltration to occur.

3.3. Capillary infiltration kinetics

Kinetics of capillary infiltration at both 180 °C and 200 °C were determined for all three PES membranes. Even within 3 min at 180 °C, effective infiltration and bonding was achieved between PES_U with PP film. The thickness of the bonded PP film/PES membrane is roughly 10 μm thinner than the sum of the PP film and the PES_U, suggesting infiltration of PP within PES pores. After soaking in chloroform overnight to dissolve the PES, the measured thickness of remaining PP film (after drying all the chloroform) was larger than the virgin PP film. In addition, surface of the PP film in contact with PES membrane became significantly rougher, and displayed vibrational signal of PES from FTIR measurements (not shown here) due to undissolved PES trapped in the infiltrated PP.

To characterize the pore structure of the infiltrated region, AFM studies were carried out on the cross-section of the bonded PP film/PES membrane. Fig. 4a shows an optical image of the microtomed sample surface, taken from the optical microscope within the AFM. A distinct tri-layer structure can be seen: the darker, dense region on the right is PP, the brighter porous region on the left is the PES membrane, and the infiltrated region (as marked) is taken to be the bonded PP film/PES_U membrane. Using AFM, a fast force map was taken across the visible tri-layer region. Fig. 4b shows topographic information from the scan. The microtomed sample surface is smooth across the dense PP film and infiltrated PP film/PES membrane regions. The un-infiltrated PES_U membrane region, on the left, is much rougher due to its porous nature and the difficulty of microtoming a porous material.

Fig. 4c shows the surface modulus map generated from the FFM scan. Here, a distinct difference can be seen between PP film (dark, softer) and PES_U membrane (light, stiffer). The porous membrane structure of PES is visible, with pores being infiltrated by PP film up to a depth of about 7–8 μm. Due to the smooth surface seen in Fig. 4b, differences in moduli between the two materials are reliable in the infiltrated region. Conversely, the roughness of the PES region renders these moduli values unreliable as height differences cause artifacts in the modulus map. The AFM data shows a modulus of about 1.6 GPa for the PES, which agrees reasonably well with literature value (2.4 GPa) [30]. In comparison, AFM measurement shows a modulus of ≈0.8 GPa for PP film, which is significantly higher than the values obtained from both DMA and tensile test (Fig. 2). The discrepancy is attributed to the difference in probing

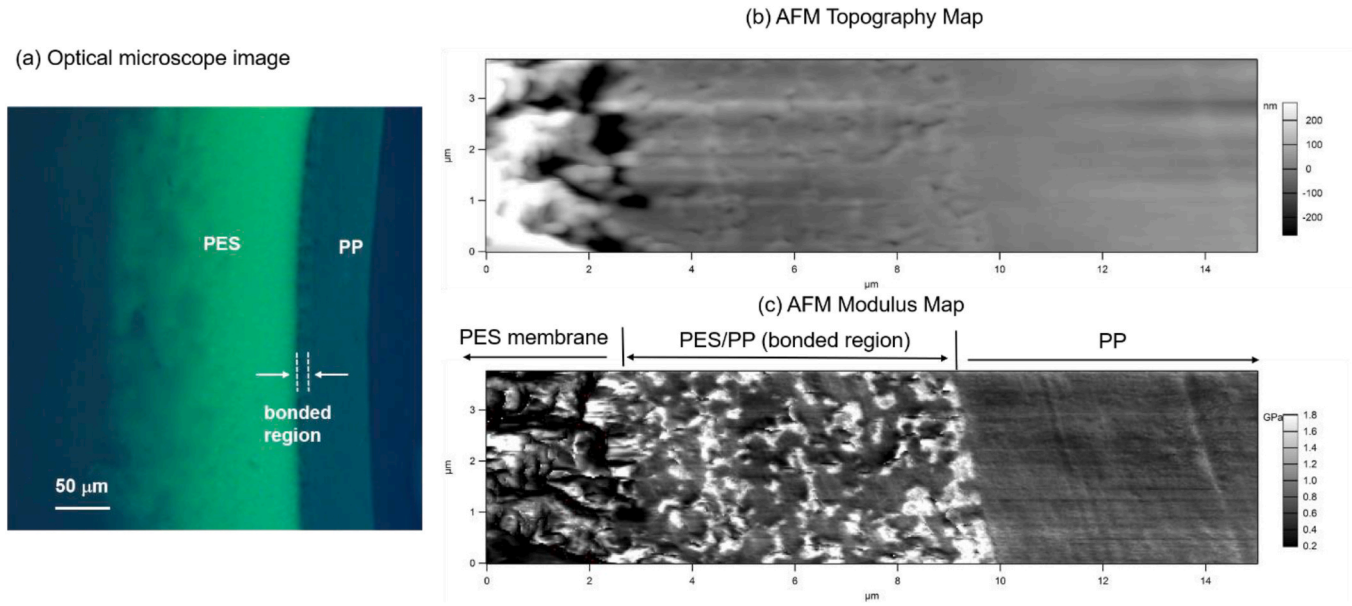

Fig. 4. (a) Optical image of the cross-section of a PES_U and PP bonded at 180 °C for 3 min, showing the tri-layer structure. (b) Topography and (c) modulus maps of the bonded PP film/PES membrane interface showing in (a).

frequency of the two methods (AFM measurement is 2 orders of magnitude faster than DMA) and the uncertainty in tip/sample contact in AFM measurements.

Importantly, Fig. 4 b and 4c show that majority of the PES pores were filled by PP film within the infiltrated region, but some void spaces (indicating partially filled pores) are still visible. The pore-saturation ratio, S_w, the ratio of the filled pores to all the pores, is estimated using image J analysis of Fig. 4c, to be 93.5%, which will be used in the analysis of the infiltration kinetics below. In addition, the infiltrated PP film preserves the PES membrane pore structure during the microtoming process. From Image J analysis, PES areal fraction was ~35%, indicating a 2D porosity of 65%. Assuming no significant in-plane variations, the volumetric porosity within the infiltrated regions are ≈65%. This surface-porosity is noticeably lower than the overall porosity (80%) of the membranes, confirming some degree of asymmetry across the membrane thickness.

For quantitative measurements of the infiltration depth, optical measurements were carried out on the microtomed PP film/PES membrane for a range of different bonding times. Given the resolution of the optical measurements and uncertainty in thermal equilibration, the infiltration time was limited to be above 3 min. Fig. 5 shows the infiltration depth as a function of time for infiltration of PP film within three PES membranes at 180 °C. With 3 min of infiltration, the infiltration depth indeed increases with the hydrophilicity of the membrane, even though the wettability of PP film on all three membranes appear similar (Table 2). However, no significant difference is observed between the three PES membranes for the overall infiltration kinetics. Complete infiltration of 180 μm thick membranes was observed for all samples within a 2 h infiltration time.

We used both LW model and Cai model to describe the experimental data, as shown in Fig. 5. For the LW model, values of η_0 θ_{PP-PES}, and γ_{PP} are all listed in Table 2, and R = 200 nm (nominal pore size) is used. Clearly, the experimentally observed infiltration kinetics are significantly slower than the LW model prediction. This discrepancy is expected given that the PES membranes have interconnected, tortuous, and non-uniform pores along the infiltration path, which is not captured in the LW model due to its cylindrical pore assumption.

In comparison, the Cai model (Eq (2)) incorporates porous media factors including tortuosity, pore size distribution, and porosity. The dash line in Fig. 5 shows the predictions of the Cai model, using identical

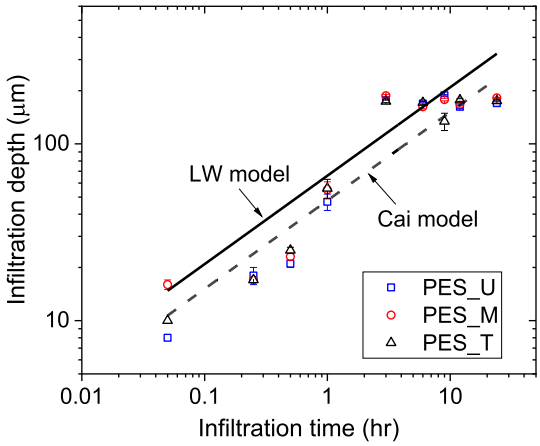

Fig. 5. Time-dependent infiltration depth for PP film in PES membranes at 180 °C. The data points are average values from measurements of three replicate samples, and the error bars represent corresponding standard deviation. The solid and dash lines represent the predictions of LW model (eq. (1)) and Cai model (eq. (2)), respectively.

materials properties, η_0, θ_{PP-PES}, γ_{PP}, as the LW model, as well as φ = 80%, $\alpha = 1$, $\tau = 1.84$, $R_{max} = 1$ μm, $S_w = 93.5\%$, $S_i = 0$, and $D_f = 1.05$. Here, φ is experimentally determined; S_w is estimated using Image J based on Fig. 4c; $S_i = 0$ because no pore-filling prior to the infiltration; value of τ is from literature report of a microporous membrane (φ = 80%, normal pore size = 200 nm) [37] that has similar pore size and porosity as membranes used in this study; D_f value (for a porous medium with $\varphi = 80\%$) is from literature [38]. Compared with the LW model, the Cai model prediction matches better with the experimental data.

It is worth noting that the Cai model does not capture the gradient in porosity and pore size distribution across the membrane thickness. As discussed earlier (Fig. 4c), the porosity near the membrane surface is lower than the overall porosity of the membrane. In addition, cross-sectional SEM (not shown) reveals qualitative increase of pore size across the membrane thickness. Experimentally determined infiltration kinetics shown in Fig. 5 is consistent with such gradient pore structure: there appears to be an acceleration of infiltration rate after 1 h when PP

reaches the depth of PES membranes with higher porosity and pore size. From modelling perspective, infiltration kinetics of membranes with such gradients in porosity and pore size can be captured by modifying Cai model with additional parameters to account for the thickness-dependent pore structure (φ and R_{max}).

Fig. 6 shows the infiltration kinetics at 200 °C. Like that observed at 180 °C, no significant difference was observed for the three PES membranes. Again, this is consistent with that fact that the wettability of PP film in the three membranes is nearly identical, as reflected in the values of θ_{PP-PES} (Table 2). Most surprisingly, the overall kinetics for the infiltration is slower than that observed at 180 °C (Fig. 5): it takes approximately 10 h at 200 °C for the PP film to completely infiltrate the three membranes compared to about 2 h at 180 °C. As infiltration temperature increases from 180 °C to 200 °C, η_0 of PP film decreases from 1650 to 290 Pa s. The driving force, capillary pressure, only decreases slightly with increase of temperature. For example, a $\frac{d\gamma}{dT} \approx 0.06$ mJ/m^2/K over 20 °C would decrease γ_{PP} by 1.2 mJ/ m^2/ K, which is a 6% reduction and is negligible compared with the 568% reduction in viscosity. If the characteristics of the porous structure of PES membranes remain identical at 200 °C, the capillary infiltration kinetics should be proportionally faster than that at 180 °C, as predicted by the Cai model (Fig. 6).

We hypothesize that this slower-than-predicted infiltration is caused by the capillary collapse of the pore structure at 200 °C. According to DMA measurements (Fig. 2b), the storage modulus of PES membrane at 180 °C is 147 MPa, identical to that at 40 °C (= 144 MPa). However, the modulus of the PES membrane starts to decrease dramatically around 200 °C (=110 MPa), reaching 10 MPa at 210 °C. Note that the modulus values from DMA measurements is at 1 Hz. During infiltration, the time scale is significantly longer than the DMA deformation rate, meaning that the effective modulus of PES membrane would be much lower. With such significant softening of PES pore walls, the capillary pressure exerted by the wetting of molten PP can cause (partial) pore collapse, which leads to significant reduction in effective pore size at the infiltration front. In well-defined lithographic structures, the critical modulus that can resist structure collapse is [39].

$$E = 24\gamma_{PP}H^4/W^3R^2 \tag{7}$$

where H and W are the effective pattern height and width and R is the distance between two neighboring structures. In the membrane pore-wetting case, H and W can be approximated as the length and thickness of the pore wall, while R is the pore diameter. Assuming H = 2 μm, W = 1 μm, and R = 400 nm, the critical modulus for pore walls to resist pore collapse (at least partially) is approximately 48 MPa, which is within the range of modulus of PES membrane at 200 °C (110 MPa) and at 210 °C (10 MPa). Assuming pore-collapsing occurs during the 200 °C-bonding, the effective pore size is expected to decrease at the meniscus of the PP, which also leads to pore shape change and increase of tortuosity. Using R_{max} = 100 nm, τ = 2, and α = 1.2 [23], the Cai model (the dotted line in Fig. 6) can adequately describe the infiltration kinetics data obtained at 200 °C.

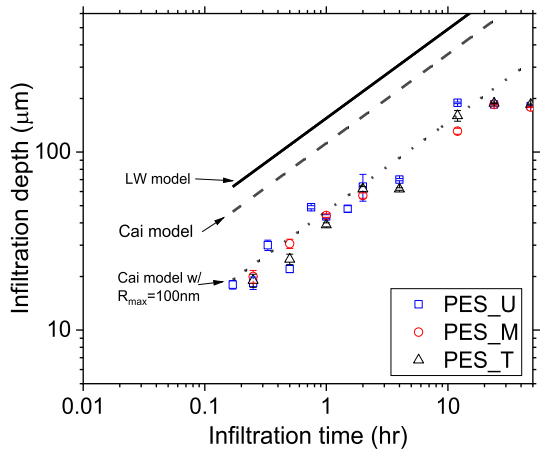

Fig. 6. Time-dependent infiltration depth for PP film in PES membranes at 200 °C. The data points are average values from measurements of three replicate samples, and the error bars represent corresponding standard deviation. Correspondingly, the solid and dash lines represent the predictions of LW model (Eq. (1)) and Cai model (Eq. (2)) using identical parameters as those for 180 °C except viscosity. The dotted line represents Cai model prediction with R_{max} = 100 nm.

3.4. Mechanical integrity of the bonded PP film/PES membranes

To understand how infiltration depth impacts the mechanical integrity of the bonded PP film/PES membrane, which is important for membrane device manufacturing, T-peel tests were performed on PP film/PES membrane bilayer samples. As shown in Fig. 7a, the unbonded regions of the PP film and PES membrane are gripped and subjected to peeling. The force-distance curves are recorded until failure. In standard T-peel tests, the force would reach a plateau corresponding to the state where the two films are steadily peeled apart [40]. Based on this steady peel force F_{peel}, one can determine the interfacial fracture toughness G_c, defined as the work required to separate a unit area of bonded interface [40]. However, such force plateau is absent in our experiments. Instead, the force first reaches a peak F_{max} and then drops to nearly zero (Fig. 7b). Examination of the bilayer samples after the test reveals that for ALL bonded PP film/PES membrane samples, failure is caused by fracture of the PES membrane before any observable debonding occurs (see the crack marked by the arrow in Fig. 7c). In addition, the PP film remains intact after the T-peel test, consistent with the fact that the strength of PP film is 3–4 times higher than that of the PES membranes (Fig. 2a). It is worth noting that other failure modes, i.e. failure between the membrane and polymer, are possible depending on the mechanical strength of the specific membrane and polymer, as well as the loading conditions. Here, although the peak force F_{max} is not directly related to the interfacial fracture toughness, it still reflects the mechanical integrity of the bonded bilayer and thus is adopted as the measure of the bonding strength.

Fig. 7d summarizes the peak force as a function of infiltration depth for all three PES membranes, bonded at both 180 °C and 200 °C. The average peak load ranges between 0.3 and 0.8 N for all the samples. Neither membrane chemistry nor bonding temperature has any significant influences over the peak force. Most interestingly, the peak load appears to decrease with increase of infiltration depth. Specifically, a linear regression of all the data in Fig. 7d results in, $F_{max} = -0.00861L + 0.85$, with a coefficient of determination of 0.67. From practical application standpoint, it is worth noting that both the infiltration depth and the peak force are outputs of the actual bonding processes and are controlled by specific bonding parameters used.

Since the failure mode is membrane fracture, the peak load reflects the effective tensile strength of the membrane under peeling, which is found to be 0.1–0.3 MPa using dimensions of the PES membrane in the T-peel samples (i.e., width = 1.43 cm and thickness = 184 μm). In comparison, the tensile strength under uniaxial tensile loading is 2.72 MPa at room temperature for as-received membrane and is 2.88 MPa after being heated at 200 °C for 1 h. Clearly, the lower effective strength observed in T-peel test is not caused by potential thermal degradation of the PES membrane. Instead, it is most likely attributed to the stress concentration could occur at the edge of the bonded/unbonded region, which is absent in uniaxial test. In particular, infiltration of PP can reduce the thickness of the remaining PES membrane, which reduces the "engineering stress", i.e. the observed peak load, at failure. Furthermore, infiltration occurs from PES membrane surface with smaller pore size and porosity. As a result, the remaining unfilled PES membranes have larger pores with higher porosity, which naturally has lower strength

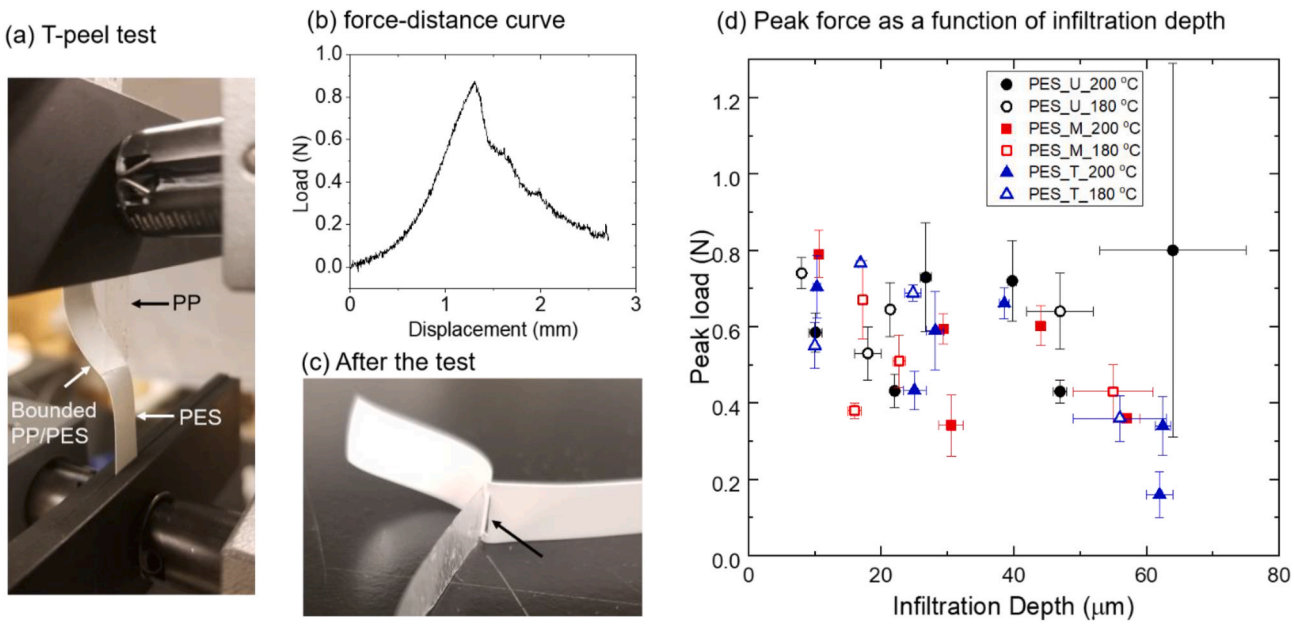

Fig. 7. (a) Photograph of a bonded PP film/PES membrane sample under a T-peel test. (b) A representative force-displacement curve, from which the peak load is determined. (c) Photograph of a PP film/PES membrane after the T-peel test. The arrow shows the fractured PES membrane. (d) Summary of peak force as a function of infiltration depth for PP film within three PES membranes: PES_U (circles), PES_M (squares), and PES_T (triangles). The filled and empty symbols represent samples infiltrated at 200 °C and 180 °C, respectively. The experimental values are average from three replicate samples and the error bars represent the standard deviation.

[27–29]. The contrast in PES membrane thickness and pore structure across the edge of the bonded/unbonded region may lead to stress concentration and hence membrane fracture.

Given that membrane fracture occurs before steady peeling, it is reasonable to assume the steady peel force F_{peel}, if membrane fracture were suppressed, should be larger than the measured peak forces (i.e., 0.3–0.8 N). This range can be used to estimate a lower bound of the interfacial fracture toughness G_c using $G_c = 2F_{peel}/W$, where W (=1.43 cm) is the width of the T-peel sample [40]. Consequently, the lower bound of G_c is estimated to be 46–123 J/m^2. The actual values of G_c can be higher but cannot be determined from our T-peel tests due to the absence of peeling. Although physically G_c is more intrinsically related to the infiltration depth, we justify adoption of the peak force as the measure of bonding strength or mechanical integrity for two reasons. First, the peak force reflects the load bearing capability of the bonded membrane and is relevant from an application perspective. Second, the definition of G_c is only valid if the infiltration depth is much smaller than the membrane thickness, otherwise one cannot define a bonded interface between the PP film and PES membrane. For example, under complete infiltration, PP film and PES membrane become completely interpenetrated without a macroscopic bonded interface.

4. Conclusions

In this study, capillary infiltration kinetics of PP film in PES membrane pores was systematically measured. PES asymmetric membranes with three surface chemistries, ranging from hydrophobic to hydrophilic were compared. The infiltration depth was determined by optical imaging of microtomed cross-sections, as a function of infiltration time for all PP film/PES membrane systems at both 180 °C and 200 °C. The results show that surface chemistry did not have any significant impact on the infiltration rate, because the PP film preferentially wet all three membrane surface chemistries. By measuring the contact angle of PP on PES, the interfacial tension of PP on PES and modified PES were estimated for the first time.

Infiltration of PP in the PES membranes was observed within minutes at 180 °C and reached the entire membrane thickness in about 2 h. The experimental data is better described by Cai model, which takes into consideration the interconnected pore structure, in comparison to the basic cylindrical pore structure used in the LW model. However, the infiltration rate at 200 °C was slower than that at 180 °C, despite that viscosity of PP film at 180 °C is 5.8 times higher than that at 200 °C. We hypothesize that the slow-than-expected infiltration at 200 °C is caused by the pore deformation/collapse of PES membrane when in contact with PP liquid due to decreased modulus of PES at 200 °C.

The mechanical integrity of the bonded PP film/PES membrane, represented by the peak load during a T-peel test, was determined. The results show that the dominant failure mode is the fracture of the PES membrane. The surface chemistry and bonding temperature did not have statistically significant impact on the peak load. Instead, the peak load decreases with increase of infiltration depth, which is consistent with the membrane failure being the dominant failure mechanism.

In this study, the infiltrating PP preferentially wets all three different PES membrane chemistries. For other infiltrating polymer/membrane combinations, surface functionalization could be a determining factor for infiltration or non-infiltration, depending on the wetting behavior. From modelling standpoint, the Cai model is expected to be effective in capturing capillary infiltration of membranes with pore size up to the capillary length of the infiltrating liquid and down to several nanometers. The understanding of capillary infiltration as well as the resulting mechanical integrity is beneficial for developing reliable membrane bonding method for device fabrication.

Declaration of competing interest

The authors declare that they have no known competing financial interests or personal relationships that could have appeared to influence the work reported in this paper.

Acknowledgment

The authors gratefully acknowledge research support from the National Science Foundation (NSF) Industry/University Cooperative Research Center for Membrane Science, Engineering and Technology (MAST) at the University of Colorado Boulder (UCB, award number, IIP 1624602). JM acknowledges support from the NSF graduate research

fellowship program (GRFP). Acknowledgment is made to the Donors of the American Chemical Society Petroleum Research Fund for partial support of this research. AB acknowledges the support from GAANN fellowship for Soft Matter.

References

[1] J.J. Keating, J. Imbrogno, G. Belfort, Polymer brushes for membrane separations: a review, ACS Appl. Mater. Interfaces 8 (2016) 28383–28399.
[2] A.Y. Kirschner, C.C. Chang, S. Kasemset, T. Emrick, B.D. Freeman, Fouling-resistant ultrafiltration membranes prepared via co-deposition of dopamine/zwitterion composite coatings, J. Membr. Sci. 541 (2017) 300–311.
[3] N. Shahkaramipour, A. Jafari, T. Tran, C.M. Stafford, C. Cheng, H.Q. Lin, Maximizing the grafting of zwitterions onto the surface of ultrafiltration membranes to improve antifouling properties, J. Membr. Sci. 601 (2020).
[4] H.-C. Yang, J. Luo, Y. Lv, P. Shen, Z.-K. Xu, Surface engineering of polymer membranes via mussel-inspired chemistry, J. Membr. Sci. 483 (2015) 42–59.
[5] S.T. Weinman, M. Bass, S. Pandit, M. Herzberg, V. Freger, S.M. Husson, A switchable zwitterionic membrane surface chemistry for biofouling control, J. Membr. Sci., 548 490-501.
[6] J. Grimaldi, J. Imbrogno, J. Kilduff, G. Belfort, New class of synthetic membranes: organophilic pervaporation brushes for organics recovery, Chem. Mater. 27 (2015) 4142–4148.
[7] S.H. Maruf, L. Wang, A.R. Greenberg, J. Pellegrino, Y.F. Ding, Use of nanoimprinted surface patterns to mitigate colloidal deposition on ultrafiltration membranes, J. Membr. Sci. 428 (2013) 598–607.
[8] O. Heinz, M. Aghajani, A.R. Greenberg, Y. Ding, Surface-patterning of polymeric membranes: fabrication and performance, Current Opinion in Chemical Engineering 20 (2018) 1–12.
[9] Y. Ding, S. Maruf, M. Aghajani, A.R. Greenberg, Surface patterning of polymeric membranes and its effect on antifouling characteristics, Separ. Sci. Technol. 52 (2017) 240–257.
[10] S.H. Fan, M. Aghajani, M.Y. Wang, J. Martinez, Y.F. Ding, Patterning flat-sheet Poly(vinylidene fluoride) membrane using templated thermally induced phase separation, J. Membr. Sci. 616 (2020).
[11] S.T. Weinman, S.M. Husson, Influence of chemical coating combined with nanopatterning on alginate fouling during nanofiltration, J. Membr. Sci. 513 (2016) 146–154.
[12] W. Goetzler, M. Guernsey, Y. Bargach, O.o.E.E.R.E. Department of Energy, in: R&D Opportunities for Membranes and Separation Technologies in Building Applications, 2017.
[13] M. Steinhart, J.H. Wendorff, A. Greiner, R.B. Wehrspohn, K. Nielsch, J. Schilling, J. Choi, U. Gosele, Polymer nanotubes by wetting of ordered porous templates, Science 296 (2002) 1997, 1997.
[14] S.L. Mei, X.D. Feng, Z.X. Jin, Polymer nanofibers by controllable infiltration of vapour swollen polymers into cylindrical nanopores, Soft Matter 9 (2013) 945–951.
[15] P.G. Degennes, Wetting - statics and dynamics, Rev. Mod. Phys. 57 (1985) 827–863.
[16] P.G. Degennes, B.W. Francoise, D. Quere, Capillarity and Wetting Phenomena: Drops, Bubbles, Pearls, Waves, sixth ed., Springer, New York, 2004.
[17] B.Y. Cao, M. Yang, G.J. Hu, Capillary filling dynamics of polymer melts in nanopores: experiments and rheological modelling, RSC Adv. 6 (2016) 7553–7559.
[18] K. Shin, S. Obukhov, J.T. Chen, J. Huh, Y. Hwang, S. Mok, P. Dobriyal, P. Thiyagarajan, T.P. Russell, Enhanced mobility of confined polymers, Nat. Mater. 6 (2007) 961–965.
[19] S. Ok, M. Steinhart, A. Serbescu, C. Franz, F.V. Chavez, K. Saalwachter, Confinement effects on chain dynamics and local chain order in entangled polymer melts, Macromolecules 43 (2010) 4429–4434.
[20] J.L. Hor, H.N. Wang, Z. Fakhraai, D. Lee, Effect of physical nanoconfinement on the viscosity of unentangled polymers during capillary rise infiltration, Macromolecules 51 (2018) 5069–5078.
[21] L.G. Cencha, R. Urteaga, C.L.A. Berli, Interferometric technique to determine the dynamics of polymeric fluids under strong confinement, Macromolecules 51 (2018) 8721–8728.
[22] J.C. Cai, B.M. Yu, M.Q. Zou, L. Luo, Fractal characterization of spontaneous Co-current imbibition in porous media, Energy Fuels 24 (2010) 1860–1867.
[23] J.C. Cai, E. Perfect, C.L. Cheng, X.Y. Hu, Generalized modeling of spontaneous imbibition based on hagen-Poiseuille flow in tortuous capillaries with variably shaped apertures, Langmuir 30 (2014) 5142–5151.
[24] F.J. Lanyi, N. Wenzke, J. Kaschta, D.W. Schubert, On the determination of the enthalpy of fusion of alpha-crystalline isotactic polypropylene using differential scanning calorimetry, X-ray diffraction, and fourier-transform infrared spectroscopy: an old story revisited, Adv. Eng. Mater. 22 (2020).
[25] M.Y. Wang, J.M. Gorham, J.P. Killgore, M. Omidvar, H.Q. Lin, F.W. DelRio, L. M. Cox, Z. Zhang, Y.F. Ding, Formation of a crack-free, hybrid skin layer with tunable surface Topography and improved gas permeation selectivity on elastomers using gel-liquid infiltration polymerization, ACS Appl. Mater. Interfaces 9 (2017) 28100–28106.
[26] A.K. Blevins, L.M. Cox, L.Q. Hu, J.A. Drisko, H.Q. Lin, C.N. Bowman, J.P. Killgore, Y.F. Ding, Spatially controlled permeability and stiffness in photopatterned two-stage reactive polymer films for enhanced CO2 barrier and mechanical toughness, Macromolecules 54 (2021) 44–52.
[27] M. Aghajani, S.H. Maruf, M. Wang, J. Yoshimura, G. Pichorim, A. Greenberg, Y. Ding, Relationship between permeation and deformation for porous membranes, J. Membr. Sci. 526 (2017) 293–300.
[28] S.H. Maruf, Z.W. Li, J.A. Yoshimura, J.L. Xiao, A.R. Greenberg, Y.F. Ding, Influence of nanoimprint lithography on membrane structure and performance, Polymer 69 (2015) 129–137.
[29] L.J. Gibson, M.F. Ashby, Cellular Solids: Structure and Properties, Cambridge university press, 1999.
[30] C.J.G. Plummer, A.M. Donald, The ductile-brittle transition in macroscopic tensile tests on polyethersulfone, J. Appl. Polym. Sci. 41 (1990) 1197–1212.
[31] A.S. Michaels, W.R. Vieth, H.H. Alcalay, Solubility parameter of polypropylene, J. Appl. Polym. Sci. 12 (1968) 1621–1624.
[32] Y.M. Wei, Z.L. Xu, X.T. Yang, H.L. Liu, Mathematical calculation of binodal curves of a polymer/solvent/nonsolvent system in the phase inversion process, Desalination 192 (2006) 91–104.
[33] D.Y. Kwok, L.K. Cheung, C.B. Park, A.W. Neumann, Study on the surface tensions of polymer melts using axisymmetric drop shape analysis, Polym. Eng. Sci. 38 (1998) 757–764.
[34] J.-S. Cho, Adhesion Aspects of Thin Films, 2005. Utrecht, The Netherlands.
[35] G.T. Dee, B.B. Sauer, The molecular-weight and temperature-dependence of polymer surface-tension – comparison of experiment with interface gradient theory, J. Colloid Interface Sci. 152 (1992) 85–103.
[36] N. Chapleau, B.D. Favis, P.J. Carreau, Measuring the interfacial tension of polyamide/polyethylene and polycarbonate/polypropylene blends: effect of temperature, Polymer 41 (2000) 6695–6698.
[37] M. Ostwal, X.Y. Lu, U. Beuscher, J. Pellegrino, Effect of microporous membrane properties and operating conditions on particle retention: measurements and model studies, Separ. Sci. Technol. 51 (2016) 1007–1021.
[38] P. Xu, B.M. Yu, Developing a new form of permeability and Kozeny-Carman constant for homogeneous porous media by means of fractal geometry, Adv. Water Resour. 31 (2008) 74–81.
[39] I. Kim, J. Mun, W. Hwang, Y. Yang, J. Rho, Capillary-force-induced collapse lithography for controlled plasmonic nanogap structures, Microsyst. Nanoeng. 6 (2020).
[40] N. Padhye, D.M. Parks, A.H. Slocum, B.L. Trout, Enhancing the performance of the T-peel test for thin and flexible adhered laminates, Rev. Sci. Instrum. 87 (2016).